Infrared temperature measurements on high pressure turbine blades in the Oxford Turbine Research Facility: calibration and image processing techniques

M. Sisti - C. Falsetti - K. S. Chana - P. F. Beard

Oxford Thermofluids Institute, Dept. of Engineering Science, University of Oxford, UK.

ABSTRACT

This paper presents the development and calibration method of an infrared (IR) measurement system to be implemented in the upgraded Oxford Turbine Research Facility. Infrared measurements will provide temperature maps on high-pressure turbine blades permitting full surface evaluation of cooling effectiveness and heat transfer coefficient at engine representative conditions. The test environment presents significant challenges for accurate IR thermography measurements. A calibration procedure to evaluate the performance of the selected IR camera, the target directional emissivity, and the transmittance of the optical path, using a combination of bespoke experimental facilities and mathematical models has been developed. The uncertainty in the calibration and an image processing method to address the blurring problem are also presented.

NOMENCLATURE

E	emissive power, $\mathrm{W\,m^{-2}}$	θ	observation angle, deg	opt	optical path
I	detector signal	α	absorptance	obj	object
c_1, c_1, c_3	fitting coefficients	ϵ	emissivity	s	surroundings
m, q	gain, offset	τ	transmittance	t	target
r, b, f	calibration constants	*Subscripts*		TC	thermocouple
R	raw digital counts	bb	black-body	c	coolant
C	influence coefficients	cam	camera	g	gas
T	temperature, K	D	detected	w	window

INTRODUCTION

A strive for high power and efficiency in jet engines led to increasing turbine entry temperatures. Thus, more efficient cooling methods are needed to ensure component life, and highly accurate temperature assessment is crucial to understand the heat transfer phenomena of high-pressure turbine components and develop novel cooling systems.

Over many years, the Oxford Turbine Research Facility (OTRF) has provided valuable highly engine-representative turbine research, and the aero-thermal measurements achieved have been used to validate computational models making them more robust and reliable for engine design. An upgrade of the facility is underway, infrared thermography is going to be used alongside more conventional techniques (e.g. themocouples, resistance temperature detectors, thin-film gauges) for heat transfer measurements. In fact, thanks to the development of high sensitivity and low response time detectors, IR thermography is now capable of assessing the temperature field in both transient and steady measurements. Infrared thermography is a high-resolution two-dimensional, non-intrusive technique however, it presents several challenges. As detailed by Falsetti *et al.* (2020), these can be summarised as: (i) conversion of the camera raw counts to an equivalent black-body temperature; (ii) target emissivity as a function of viewing angle, and surface condition; (iii) transmittance of the optical path; (iv) reflection from surroundings.

In the early '90s, the calibration of an IR thermography system to obtain quantitative results was starting to be addressed. Martiny *et al.* (1996) and Schulz (2000) developed $in-situ$ calibration methods using reference thermocouples embedded into the test surface and a semi-empirical equation

for Planck's Law to obtain the following calibration function:

$$T_{obj} = \frac{b}{ln(\frac{r}{I_{obj}} + f)} \tag{1}$$

where I_{obj} is the signal emitted by the target. Later, Ochs *et al.* (2009) proposed a novel semi $in - situ$ calibration method that improved the accuracy and also considered the impact of the optical access window. The signal I_{obj} in Eq. 1 was explicitly expressed as the difference between the total detector signal and the offset signal, I_{offset}, consisting of the radiance emitted by the surroundings and reflected by the target. The parameters r, b, f, and I_{offset} were pre-estimated during an off-line calibration performed at steady ambient temperature. Subsequently, a second stage $in - situ$ calibration focused on studying the effect of the optical path on the total spectral transmittance and re-calibration the offset signal. The maximum errors in the temperature readings were reduced from 12% (Martiny *et al.*, 1996) to 1.2% of the temperature span tested.

More recently, Kirollos and Povey (2015) presented a grey-body calibration to evaluate the transmittance of the optical path, the emissivity of the target, and the surroundings and the optical path temperatures. The grey-body calibration was performed $in - situ$ using a surrogate radiance correction vane. Kirollos and Povey (2017) also developed a calibration for situations with important spatial variation in reflection from surroundings or in viewing angle. The authors applied a reflective marker array (RMA) on the target surface and used an advanced image analysis to estimate the surroundings temperature and the emissivity. The method reduced the maximum error in the temperature from $6°$C (conventional method) to $1.5°$C for object temperatures in the range of $38°$C to $56°$C. Elfner *et al.* (2017, 2018) corrected for directional emissivity with a custom bi-directional reflectance function (BRDF). The detector radiation was corrected with $\epsilon(\theta)$ using a linear relation. Results showed that the maximum uncertainty on a flat surface was $\pm\, 0.3$ K. The residual uncertainty for the angular dependency of emissivity was equal to $\pm\, 0.67$ K for viewing angles lower than 50 deg, while it increased up to $\pm\, 3.19$ K at angles of 70 deg. The results confirmed what other studies concluded on the negligible influence of observation angles below 55 deg (Manara *et al.*, 2017; Holgate *et al.*, 2019).

In a following study, Elfner *et al.* (2019) further improved the calibration developed by Ochs *et al.* (2009). The offset radiance, I_{offset}, was considered as the main source of error. The authors defined a non-dimensional correction field, $C = f(\overrightarrow{x})$, representing the magnitude of I_{offset} to evaluate its spatial variation. The uncertainty in the surface temperature reduced from 8% to approximately 2% at a test temperature of 350 K.

Infrared thermography has been widely used in turbine heat transfer research albeit limited to stationary experiments. Only few studies have addressed the application of IR thermography onto rotating facilities. One of the first was presented by Lazzi-Gazzini *et al.* (2017), who used IR thermography to evaluate the heat loads of an axial turbine rotor endwalls at $2,700$ rpm. More recently, Christensen *et al.* (2020) reported on IR thermography used to measure blade tips temperatures at $13,000$ rpm. Finally, Knisely *et al.* (2021) looked into the different effects that influence IR detector performance in measuring temperatures of rotating blades. These studies have also shown that image post-processing plays a fundamental role in generating results. Lazzi-Gazzini *et al.* (2017) developed image processing technique to solve the measurement challenges associated with the target velocity by combining two sets of images taken at two different integration times; Christensen *et al.* (2020) developed a de-blurring algorithm to process IR blade tip temperature data. Studies on similar image post-processing can be found in other optical technique research, Gregory *et al.* (2014) reported on de-blurring methods for pressure sensitive paint measurements on rotating surfaces.

This paper presents the development of a novel calibration technique to improve the accuracy of IR measurements when applied to fast moving targets. The calibration is performed by using two experimental facilities: (i) a rotating disc facility, used to estimate the effect of speed and temperature on the quality of IR images, and (ii) a black-body calibration facility, used to evaluate the directional emissivity and the transmittance of the optical window.

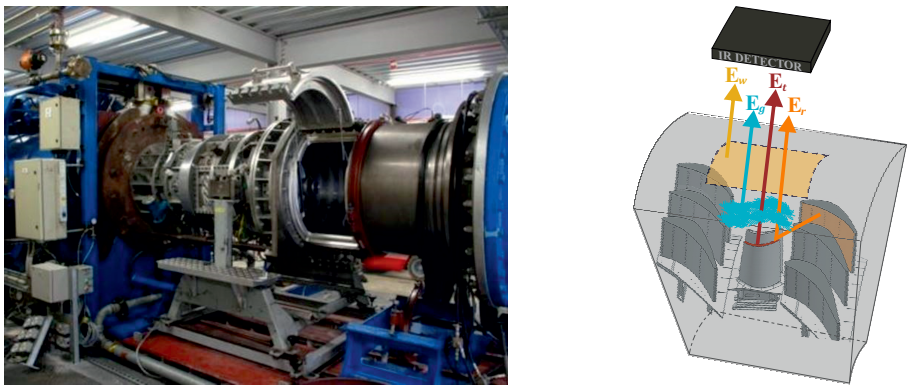

(a) (b)

Figure 1: (a) Photograph of the OTRF, (b) different radiation contribution reaching the IR detector.

INFRARED CAMERA MEASUREMENTS IN THE OTRF

The Oxford Turbine Research Facility is a short duration light piston facility, capable of testing single or 1.5 stage cooled high-pressure turbines. A photograph of the OTRF is shown in Fig. 1(a). The facility is capable of matching engine representative conditions for Mach and Reynolds numbers, non-dimensional speed and gas-to-wall temperature ratio. A cumbustor simulator is also implemented (Adams *et al.*, 2020). Chana *et al.* (2013) detailed the facility operation and presented a review of published research. An upgrade to the OTRF is underway to permit a semi-transient test mode with an extended run time of up to 60 s, enough for the turbine components to reach thermal stability (time constant $\sim$ 5 s). As part of this upgrade an IR system will be implemented to permit full surface measurement of cooling effectiveness and heat transfer coefficient on the rotor blade surfaces, platforms and casing walls.

The OTRF testing conditions make the design and implementation of an IR thermography system for rotor blade temperature measurements a challenging task. In fact, the maximum rotational speed of $10,000$ rpm, that translates into $\sim$ 250 $\mathrm{m\,s^{-1}}$ rotor blade tangential velocity, adds an ulterior complication. To achieve high accuracy measurements, a thorough understanding of infrared radiation and the main sources of error is required, and the calibration technique needs to be fine-tuned to the expected test conditions.

An illustration highlighting the different radiation contributions acquired by an IR detector in a typical turbine IR thermography system is shown in Fig. 1(b) (Falsetti *et al.*, 2020). The radiation reaching the detector can be expressed as the sum of that emitted by the target and transmitted by the optical path ($\tau_{opt}\epsilon_t E_t$), and a certain amount of disturbance radiation (E_{offset}):

$$E_{cam} = \tau_{opt}\epsilon_t E_t + E_{offset} \tag{2}$$

The disturbance radiation, E_{offset}, is the sum of: i) the radiation emitted by the surroundings (E_s), which is first reflected on the target surface due to its reflectivity ($1-\epsilon_t$) and then attenuated by the optical path transmittance (τ_{opt}); ii) the radiation emitted by the optical path, which is in turn the sum of the radiation emitted by the mainstream gases (E_g), and the radiation emitted by the IR-transparent window (E_w). Thus, using the *Stefan-Boltzmann* equation, Eq. 2 can be rewritten in terms of temperature and solved for the target temperature T_t:

$$T_t^4(x,t) = \frac{T_{cam}^4(x,t) - \tau_{opt}(1-\epsilon_t(x,\theta))T_s^4(x,t) - (1-\tau_{opt})T_{opt}^4(t)}{\tau_{opt}\epsilon_t(x,\theta)} \tag{3}$$

where T_{cam} is the equivalent black-body temperature measured by the IR camera, T_s is the surroundings temperature and T_{opt} is the temperature of the optical path (turbine working fluid and window). Eq. 3 shows that the radiation detected by the camera is not only related to the target temperature, thus measurement or estimation of the target emissivity, the optical path transmittance and the disturbance radiation is required.

Table 1: Influence coefficients C_i of each variable to the final T_t of expected value 500 K.

Variable		Expected Values	C_i
Equivalent black-body temperature	T_{cam}	506 K	1.311
Target Emissivity	ϵ_t	0.86	0.145
Optical Path Transmittance	τ_{opt}	0.95	0.051
Surroundings Temperature	T_s	550 K	0.211
Optical Path Temperature	T_{opt}	470 K	0.0175

Calculating error caused by the disturbance radiation is not straightforward, as the temperature distributions of the surrounding surfaces are not isothermal, and view factors must be estimated. Nevertheless, from inspection of Eq. 3 it is clear that the reflected radiation from the surroundings is reduced for a target with high emissivity. Hence to minimise the correction due to the surroundings radiation, it is common to coat the target with a thin layer of high emissivity paint (typically 0.9 to 0.97), especially when the target has a low emissivity such as the metal alloys used in gas turbines. The paint used in this study is the RS Matt Black Paint.

In most turbomachinery applications, the optical path is composed of the test gas and IR transparent window used to gain optical access. The absorption of the test gas is mainly due to water vapour and CO_2 (Gao *et al.*, 2015) however, the test gas in the OTRF is dry air with atmospheric levels of CO_2 hence the absorption can be considered negligible. Ochs *et al.* (2009) determined that in the IR camera sensitive spectral bandwidth, τ_{opt} can depend on temperature and wavelength of incident radiation. Therefore careful consideration must be paid on the choice of window material. Given its transmittance insensitivity to temperature and wavelength in the IR camera wavelength range, Zinc Selenide (ZnSe) was used in this study. The window is coated to reduce back reflection and ghost image formations yielding highly efficient transmissive optics.

In order to estimate which parameter has a larger impact on the evaluation of the target temperature, a sensitivity analysis was carried out based on Eq. 3. The influence coefficients, C, are obtained by changing each variable (T_{cam}, ϵ_t, τ_{opt}, T_s, and T_{opt}) of $1\,\%$ and re-calcutating the new target temperature, as $C_i = (T_t - T_{t,i})/(T_t) \cdot 100$. This describes how the target temperature varies when each variable changes by $1\,\%$. This method requires knowing the expected values of each variable. The temperatures (T_t, T_s, and T_{opt}) are assumed considering previous experiments in OTRF, ϵ_t and τ_{opt} are measured via calibration, as explained in the following sections, and T_{cam} is calculated using Eq. 3. The results are outlined in Table 1.

Based on the results of this analysis, it is clear that particular attention must be given when estimating all the variables to ensure an accurate measurement and ideally traceable uncertainty evaluation.

In the following sections, first the experimental facility and the triggering system developed for testing the camera performance are described. Subsequently, the experimental calibration is detailed. Lastly, the image deblurring method is outlined. As the first planned OTRF tests focus on tip heat transfer, the surroundings reflection, and hence the influence of T_s, are not considered in this study.

IR CAMERA SELECTION & PERFORMANCE EVALUATION

The choice of IR camera and lens considered the expected measurement temperature range, field of view, working distance and target velocity. Primarily, the high relative velocity of the target required a fast IR detector capable of capturing sufficient signal at very low integration times to obtain sharp images (limited blade displacement per pixels). A FLIR A6751SLS IR camera was chosen for its extremely short integration times that can be set down to 0.48 μs. The camera features a 640 x 512 resolution, Strained Layer Superlattice (SLS) detector, and a maximum frame rate at full window of 125 Hz.

Experimental testing of IR camera performance

A rotating disc facility was designed to evaluate the camera performance at conditions similar to the OTRF and to develop the camera triggering system. The facility consists of an aluminum 6082

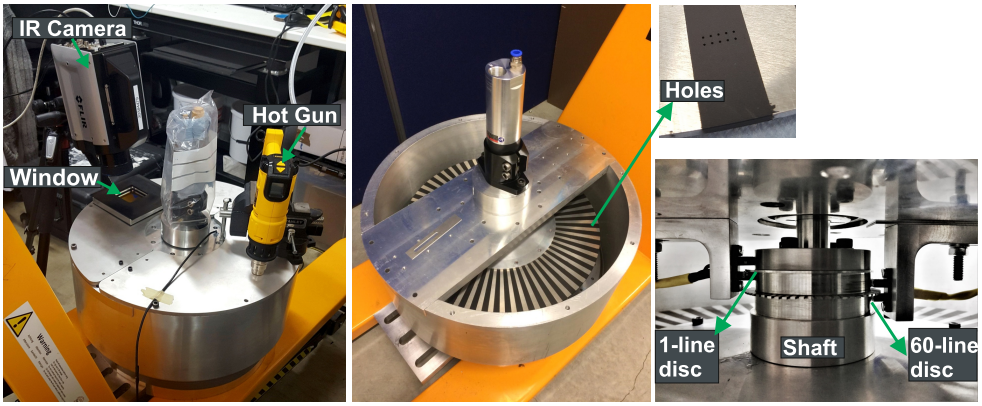

Figure 2: Rotating disc facility, with zoom on the encoder installation on the shaft.

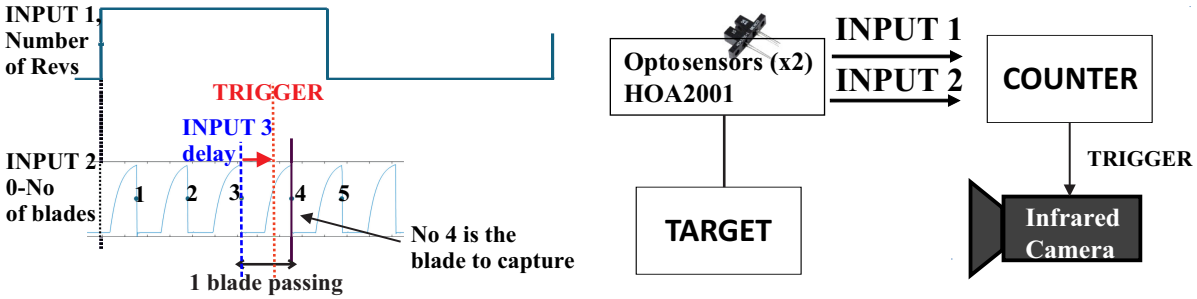

Figure 3: IR camera triggering system block diagram.

T6 disc, with a diameter of 450 mm, driven by an air motor up to 8000 rpm, as shown in Fig. 2. A cylindrical enclosure houses the disc and optical access is gained through a ZnSe window. A hot air blower heats up the disc to a temperature of $\sim$ 330 K. Stripes of high emissivity RS Matt Black paint sprayed onto the disc simulate 60 rotor blade passing events, with two stripes including 0.5 mm diameter hole arrays to simulate film cooling holes. The facility shaft includes 1-line and 60-line optical encoders. The first measures disc rotational speed (rpm), whilst the second provides rotary position with respect to the simulated rotor blades (i.e. the black stripes).

Camera triggering system

Experimental campaigns in the OTRF may include testing of multiple blade cooling designs in a single rotor build. To reduce facility down time, an IR thermography measurement capable of acquiring thermal images on any rotor blade without modification to the test facility hardware is required. To achieve this, a camera triggering system has been developed. A block diagram of the system is shown in Fig. 3. The signals from the two optical encoders are acquired by a National Instruments NI-9402 digital module, programmed with LabVIEW to trigger the IR camera. The 1 line optical encoder signal (input 1) is used to reset the system, allowing the user to choose the number of rotor revolutions between image capture. A counter determines blade passing events based on the 60 line optical encoder signal (input 2). When this counter reaches the user defined blade number, image capture is triggered. A programmable delay (input 3) allows for any delay in the camera response and fine tuning of the blade position relative to the camera at the time of image capture. For example, different delay settings would be selected to view the pressure surface, suction surface or rotor tip, while optimising the viewing angle.

Infrared images as a function of disc temperature and speed

A measurement campaign was performed in the rotating disc facility to ascertain the impact of speed and temperature on the quality of IR images. An IR image of the disc at approximately 45°C without rotation is shown in Fig. 4(a). The importance of high emissivity coating to minimise distur-

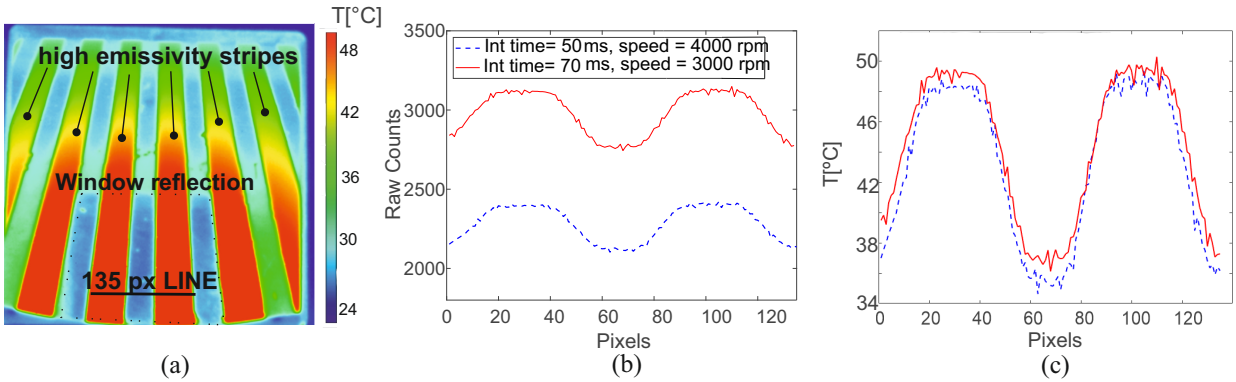

(a) (b) (c)

Figure 4: (a) IR image of steady disc heated to ~ 45°C, (b) raw counts along a 135 pixels line and (c) corresponding temperature values.

bance radiation is undeniable; the regions without the coating present a high level of reflection from surroundings and from the optical window, while the coated sectors present a uniform temperature near the outer radius. The radial temperature distribution that goes from ~ 45°C to 35.5°C along the painted stripes is explained by the presence of non-uniform heating (hot air blower targeted on disc outer radius) and the dependence of surface emissivity on the observation angle, which was higher than 55 deg for this particular test.

Two example results, taken at the same disc temperature (~ 50°C) and different rotational speed and integration time (3000 rpm and 70 μs, and 4000 rpm and 50 μs), are shown in Fig. 4(b) and (c). The results present raw signal counts (Fig. 4(b)) and temperature (Fig 4(c)) obtained along a line of 135 pixels covering two stripes, identified by the horizontal black line in Fig. 4(a). The difference of signal between high-emissivity and un-coated regions is clearly visible. As expected, the raw signal count decreases with integration time.

CALIBRATION METHOD

A bespoke facility has been developed to perform the calibration of the IR camera against a black-body and to evaluate directional surface emissivity and transmittance of the optical path. A CAD model of the bespoke calibration facility is shown in Fig. 5. An enclosure manufactured from black matt finish Foamex PVC is used to shield the calibrator and the camera from stray radiation. Therefore, it aids signal stability, which could be disturbed by ambient temperature fluctuation. The facility length permits testing over a large range of camera/target relative distances. A breadboard base and a rotating breadboard are used to adjust camera and target relative position.

In this section, the IR camera calibration method is detailed. This approach includes three separate calibration experiments: a detector calibration, a directional surface emissivity calibration, and a transmittance calibration. The uncertainty in the calibration procedure is also presented.

Detector calibration

The FLIR A6751 SLS IR camera detector consists of a 640x512 pixels array (Focal Plane Array, FPA). Two main steps are necessary to determine the final temperature map from the measured raw signal: a non-uniformity correction (NUC) and a radiometric calibration. The data used for the detector calibration were obtained by uniformly irradiating the FPA with a black-body source at different temperatures T_{bb}, and by averaging 100 frames measured at 125 Hz. In the calculation presented below, the subscript i indicates the black-body temperature step, while the subscripts y, x indicate the pixel location in the array.

Non-Uniformity Correction

Despite the uniform irradiation, the pixel array gives a non-uniform response. The first step of the detector calibration aims at correcting this non-uniformity. The correction hereby presented follows

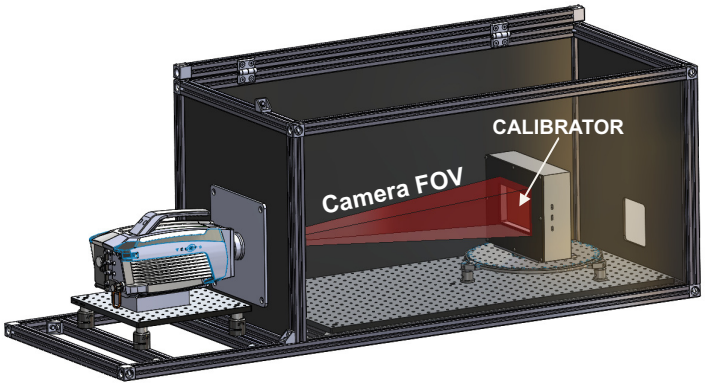

Figure 5: CAD model of the facility used for the calibration.

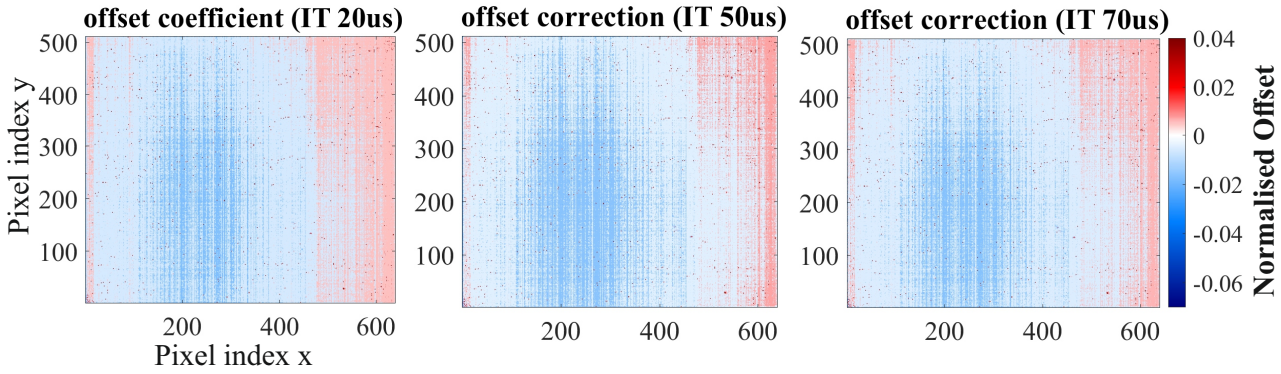

Figure 6: Normalised offset maps for different integration times.

the procedure detailed by Schulz and Caldwell (1995). The relationship between the signal deviation of each pixel $\Delta R_{y,x}$ from the mean signal over the entire FPA $\langle R \rangle$ and the mean signal is linear and can be described as follows:

$$\Delta R_{i,yx} = m_{yx} \langle R_i \rangle + q_{yx} \tag{4}$$

The coefficients m_{yx} and q_{yx}, namely the $gain$ and the $offset$, are calculated for each pixel by curve fitting. Figure 6 shows the offset maps normalised by the dynamic range for three different integration times, these are very similar in pattern and magnitude. The offset varies between 0.0011 ± 1.0626 for $20\,\mu s$, 0.0012 ± 1.0751 for $50\,\mu s$, and 0.0014 ± 1.0322 for $70\,\mu s$. The gain varies between $2.9193 \cdot 10^{-7} \pm 1.2229 \cdot 10^{-4}$ for $20\,\mu s$, $3.2989 \cdot 10^{-7} \pm 1.2014 \cdot 10^{-4}$ for $50\,\mu s$, and $2.7019 \cdot 10^{-7} \pm 1.1833 \cdot 10^{-4}$ for $50\,\mu s$. Finally, the corrected signal is obtained as follows:

$$R^c_{i,yx} = \frac{R_{i,yx} - q_{yx}}{1 + m_{yx}} \tag{5}$$

The corrected signal will then be used to perform the radiometric calibration detailed in the following section.

Radiometric Calibration

The radiometric black-body calibration relates the corrected pixel digital count ($R^c_{i,yx}$) to the temperature of the black-body source (T_{bb}). The FLIR A6751 SLS IR camera was factory calibrated for an integration time of 0.112 ms. Generally, it is good practice to repeat the calibration in laboratory environment, however, this is absolutely necessary if different integration times are to be chosen.

The radiometric calibration was carried out for three integration times: $20\,\mu s$, $50\,\mu s$ and $70\,\mu s$. Two black-body sources were used, the CI-Systems SR33-7 and the Fluke 4181. Both are calibrated to an international standard. The calibration temperatures go from 20°C to 270°C, covering the expected experimental temperature range. The CI-Systems calibrator was used for temperature between 20°C

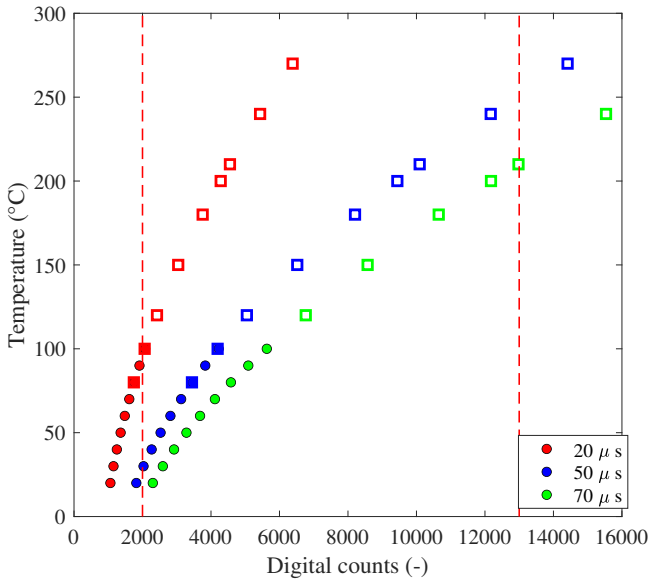

Figure 7: Digital counts vs temperature for three integration times. The data indicated by the dots is measured with the CI calibrator, the squares indicate the data measured with the Fluke calibrator.

and 100°C, and the Fluke 4181 between 100°C and 270°C, due to their lower uncertainty in those ranges.

A pixel-by-pixel calibration was performed and the calibration constants c_1, c_2, c_3 were determined using a second order polynomial fit, as follows:

$$T_{cam,i} = c_{1,yx} {R^c_{i,yx}}^2 + c_{2,yx} R^c_{i,yx} + c_{3,yx} \tag{6}$$

The experimental data are shown in Fig. 7 for one specific pixel and different integration times. The two vertical dotted lines in Fig. 7 indicate the camera manufacturer recommended minimum and maximum fill level, 12% and 82% respectively. A very low integration time would remove the blur however, if the minimum fill level is not reached, noise would start dominating and the image would have poor temperature resolution. It can be inferred from Fig. 7 that for temperatures below 90°C, the minimum admissible integration time is 50 μs, where the detector saturation is 23% at 90°C and decreases to 12% at 20°C. At temperatures higher than 90°C, the integration time can be reduced to 20 μs, as the detector saturation is 13%. A shorter integration time of 10 μs is achievable if the target temperature is above 150°C.

The uncertainty on the camera temperature, $U_{T_{cam}}$, is the result of the combined error from the reference black-body source, i.e. the calibrators, and the error from Eq. 6. The results of the uncertainty analysis are obtained for four different temperatures of the black-body source, between 50°C and 200°C, as outlined in Table 2. The uncertainty on the black-body temperature, $U_{T_{bb}}$, comes from the root sum squared of the calibrators accuracy, stability and uniformity. The error of the curve fitting was quantified by the RMS error, which defines the mean absolute error of the residuals.

Table 2: Detector calibration uncertainty analysis.

		50°C	100°C	150°C	200°C
$U_{T_{bb}}$	Black-body calibrator, °C	±0.25	±0.57	±0.73	±0.88
$U_{fitting}$	rmse, °C	±0.42	±1.14	±1.14	±1.14
$U_{T_{cam}}$	IR camera, °C	±0.5	±1.27	±1.35	±1.44

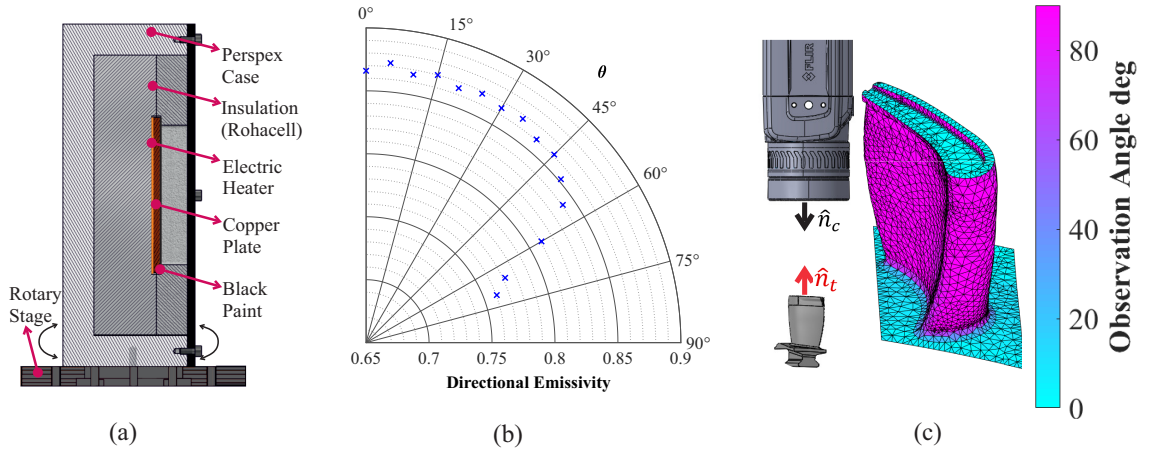

(a) (b) (c)

Figure 8: (a) Sketch of the calibration plate, (b) polar plot of directional emissivity, (c) observation angles computed considering the camera perpendicular to the blade tip.

Directional Surface Emissivity Calibration

The directional surface emissivity of the coating applied to the OTRF turbine components was calibrated using the set-up outlined in Fig. 7(a). This consists of a rectangular copper plate (150 mm x 100 mm) coated with RS Matt Black spray and heated by an electrical silicone heater mat mounted on its back surface. To achieve isothermal conditions, the plate was sandwiched between two layers of ROHACELL® ($k \approx 0.03 \mathrm{W\,m^{-1}\,K^{-1}}$) and inserted into a Perspex® casing. The target was supported by a rotating mount and the directional emissivity was calibrated between 0 deg and 70 deg. Eight surface mounted T-type thermocouples (four on the front and four on the back side of the copper), determined the temperature uniformity of the copper plate and were used as reference for the calibration. The IR camera measured the temperature of the copper plate in a region close to the thermocouples locations. The directional emissivity was calculated as:

$$\epsilon(\theta) = \frac{T_{cam}^4(\theta) - T_S^4}{T_{TC}^4 - T_S^4} \tag{7}$$

where T_{cam} and T_{TC} are the temperature of the copper plate measured by the IR camera and thermocouple respectively. The surroundings temperature, T_S, was maintained equal to ambient conditions and measured by a thermocouple. The directional emissivity values are illustrated in Fig. 7(b). This was found to be approximately constant and equal to 0.86 up to angles of 50 deg when it starts decreasing, reaching 0.75. The uncertainties on the directional emissivity, U_ϵ, are the result of the errors propagation associated with Eq. 7, see Table 3.

A MATLAB code was developed to calculate the observation angles for more complicated geometries, such as blades. The code reads the mesh file of the CAD, computes the normal vectors to the geometry surfaces and the angle between these and the normal vector to the camera. An example is shown in Fig. 7(c).

Table 3: Emissivity calibration uncertainty analysis.

		50°C	100°C	150°C	200°C
$U_{T_{TC}}$, U_{T_S}	T-type thermocouple, °C	±0.5	±0.5	±0.6	±0.76
$U_{T_{cam}}$	IR camera, °C	±0.5	±1.27	±1.35	±1.44
U_ϵ	Emissivity	±0.03	±0.02	±0.02	±0.01

Transmittance Calibration

The final step in the calibration was to characterise the optical path influence on the signal detected by the IR camera. The optical path is composed of the test gas and the IR transparent window. The test gas transmittance in the camera working wavelength is approximately 1 (Gao *et al.*, 2015). Thus, the

source that mainly affects the optical path transmittance is the IR window. The spectral transmittance of a 10 mm thick ZnSe optical window with anti-reflective coating was determined. The CI-System black-body source was used as reference body and the window was placed between the calibrator and the camera. The transmittance was calculated as:

$$\tau = \frac{T_{cam}^4(\theta) - T_{opt}^4}{T_{bb}^4 - T_{opt}^4} \tag{8}$$

where T_{cam} is measured by the camera, T_{bb} is the black-body source temperature and T_{opt} the optical path temperature, measured by a T-type thermocouples and maintained at ambient condition during the calibration. The window transmittance was calculated at different black-body temperatures, $50°$C and $70°$C, and was found to be $\tau = 0.95$. The uncertainties on the transmittance, U_τ, are the result of the errors propagation from Eq. 8, see Table 4.

Table 4: Transmittance calibration uncertainty analysis.

		50°C	100°C	150°C	200°C
$U_{T_{bb}}$	Black-body calibrator, °C	±0.25	±0.57	±0.73	±0.88
$U_{T_{opt}}$	T-type thermocouple, °C	±0.5	±0.5	±0.6	±0.76
$U_{T_{cam}}$	IR camera, °C	±0.5	±1.27	±1.35	±1.44
U_τ	Transmittance	±0.02	±0.02	±0.02	±0.01

Uncertainty Analysis in Target Temperature and Cooling Effectiveness

The ultimate goal of the IR system hereby presented is to assess cooling effectiveness, which is the criterion generally used to compare different cooling designs, defined as:

$$\eta = \frac{T_t - T_c}{T_g - T_c} \tag{9}$$

where the target temperature, T_t, is obtained using IR thermography according to Eq. 3, T_c and T_g are coolant and gas temperatures respectively.

The expected measurement (bias) uncertainties in T_t and η have been calculated for target (blade) temperatures ranging from 100 - 200°C, corresponding to cooling effectiveness values of 0.45-1.0 for a typical OTRF test. This analysis is summarised in Table 5 using typical errors in coolant temperature (±1 K) and rotor inlet gas temperature (±2.5 K). In absolute terms, the bias errors in T_t range from ±1.49°C to ±1°C with a consistent error in η of approximately ±0.02. Precision, or repeatability, errors are not presented in this pre-test analysis but are expected to be an order of magnitude lower than the presented bias errors. The repeatability uncertainty would represent the ability of the measurement system to determine changes in cooling effectiveness values at different turbine operation conditions or between different blade cooling technologies.

Table 5: Cooling effectiveness uncertainty analysis.

T_t	Blade temperature	100°C	125°C	150°C	175°C	200°C
η	Cooling effectiveness	0.46	0.59	0.73	0.87	1
U_{T_t}	IR themography, °C	±1.49	±1.23	±1.02	±1	±1
U_η	Cooling effectiveness	±0.03	±0.02	±0.02	±0.02	±0.02

IMAGE POST PROCESSING

In order to perform accurate IR measurements of a high-speed target and reduce the blur in the image, it is essential to find the right balance between the intensity reaching the detector and the integration time. The radiometric calibrations shown in Fig. 7 were used for this purpose. The results suggest the acquisition of images at two integration times, $20\,\mu s$ and $50\,\mu s$. The lower integration

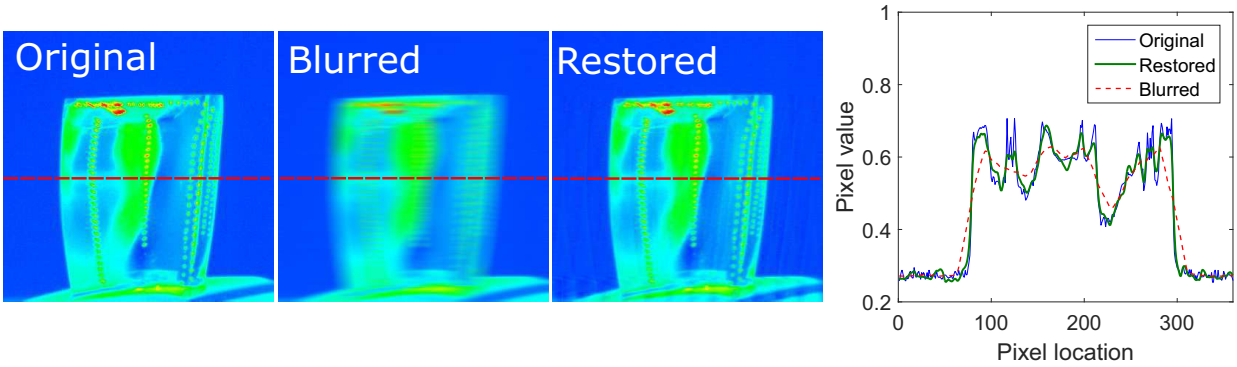

Figure 9: Effect of the horizontal motion blur and restoration algorithm. The pixel values from 0 to 1 of the horizontal red dotted line are obtained considering the corresponding black and white figures.

time minimises the blur caused by the displacement, while the higher integration time ensures an acceptable temperature resolution. The two sets of images will then be processed and combined to obtain the correct temperature and deblurring, as done by Lazzi-Gazzini *et al.* (2017).

Given the working distance, camera resolution and rotor speed it is possible to estimate the blur in terms of pixels, obtaining 12 and 30 pixels for integration time of $20\,\mu s$ and $50\,\mu s$ respectively. The blur caused by the blade tip movement can be considered uniform across all the pixels. Consequently, the point-spread function (PSF), h, may be assumed invariant and it is calculated with the MATLAB function $fspecial$. The blurred image, b, is expressed by a convolution of h with the exact sharp image x (Hansen *et al.*, 2006):

$$b = h \otimes x \tag{10}$$

Equation 10 can be rewritten in the frequency domain using the discrete Fourier transforms of the real image ($\hat{\mathbf{X}}$), the blurred image ($\hat{\mathbf{B}}$), and the PSF ($\mathbf{H}$). Since this operation is prone to numerical instabilities that amplify the high-frequency noise components, a filtering is required. This is performed by adding a noise term, which leads to the following equation in the Fourier domain (Gonzalez and Woods, 1992):

$$\hat{\mathbf{X}} = \frac{\hat{\mathbf{B}}}{\mathbf{H}} = \left[\frac{1}{\mathbf{H}}\frac{\mathbf{H}^2}{\mathbf{H}^2 + \gamma(S_n/S_x)}\right]\hat{\mathbf{B}} \tag{11}$$

In this study, the deblurring process is performed by implementing the estimated PSF and a Wiener filter, using the MATLAB function $deconvwr$. In order to analyse the performance of the deblurring algorithm, a synthetic blur of 30 pixels was added to a steady image of a blade and then removed using the restoration algorithm, as shown by the examples in Fig. 9. The image is reconstructed correctly, as also highlighted by the pixel values plot: the restored pixel values (green line) reconstruct the position of the blade edges (at pixel locations 75 and 300) and of the cooling holes near the leading edge (at pixel locations 255, 275 and 285) correctly. On the contrary, the blurred image smears the location and pixel intensity of the cooling holes. The root mean square error between original and blurred image is equal to $\sim 11\%$. This error is reduced to $\sim 3\%$ thanks the restoration process and, translated in the temperature field, leads to an uncertainty of 2.5 K.

CONCLUSION

This paper presents a novel calibration method for a high-accuracy IR measurements to be used in the Oxford Turbine Research Facility with fast moving targets.

A pixel by pixel calibration and techniques to characterise the directional emissivity and transmittance were performed with bespoke facilities. The emissivity was calibrated with an uncertainty that ranges from ± 0.03 to ± 0.01, while the transmittance uncertainty ranges from ± 0.02 to ± 0.01. The calibration results demonstrate that the absolute expected uncertainty on the target temperature varies

from ± 1.49°C at $T = 100$°C to ± 1°C at $T = 200$°C. These would translate into a consistent uncertainty in cooling effectiveness of approximately ± 0.02. The proposed image restoration reduces the errors due to blurring from 11% to 3%. A novel infrared measurement calibration technique has been developed to obtain high-resolution thermal images in the OTRF. Future work will aim at optimising the image restoration method and estimating the effect of surroundings reflections. This technique will provide valuable and accurate cooling effectiveness and heat transfer data helping to guide the design of future more efficient turbine components and cooling technologies.

References

M.G. Adams, T. Povey, B.F. Hall, D.N. Cardwell, K.S. Chana, and P.F. Beard. Commissioning of a combined hot-streak and swirl profile generator in a transonic turbine test facility. *Journal of Engineering for Gas Turbines and Power*, 142, 2020.

K.S. Chana, D.N Cardwell, and T.V. Jones. A review of the oxford turbine research facility. *Proceedings of the ASME Turbo Expo*, 3, 06 2013. doi: 10.1115/GT2013-95687.

L. Christensen, R. Celestina, S. Sperling, R. Mathison, H. Aksoy, and J. Liu. Infrared temperature measurements of the blade tip for a turbine operating at corrected engine conditions. *Proceedings of the ASME Turbo Expo*, 7, 9 2020.

M. Elfner, A. Schulz, H-J. Bauer, and K. Lehmann. A novel test rig for assessing advanced rotor blade cooling concepts, measurement technique and first results. *Proceedings of ASME Turbo Expo 2017: Turbomachinery Technical Conference and Exposition, Charlotte, USA*, pages 1–12, 2017.

M. Elfner, A. Schulz, H-J. Bauer, and K. Lehmann. Comparative experimental investigation of leading edge cooling concepts of turbine rotor blades. *Proceedings of ASME Turbo Expo 2018: Turbomachinery Technical Conference and Exposition, Oslo, Norway*, pages 1–12, 2018.

M. Elfner, T. Glasenapp, A. Schulz, and H-J. Bauer. A spatially resolved in situ calibration applied to infrared thermography. *Meas. Sci. Technol.*, 30:1–10, 2019.

C. Falsetti, M. Sisti, and P.F. Beard. Infrared thermography and calibration techniques for gas turbine applications: a review. *Infrared Physics and Technology*, 2020.

S. Gao, L. Wang, C. Feng, and K.D. Kipngetich. Analyzing the influence of combustion gas on a gas turbine by radiation thermometry. *Infrared Phys. Technol.*, 79:184–193, 2015.

R.C. Gonzalez and R.E. Woods. *Digital Image Processing*. Addison-Wesley, Reading, MA, 1992.

J.W. Gregory, K.J. Disotell, D. Peng, T.J. Juliano, J. Crafton, and N.M. Komerath. Inverse methods for deblurring pressure-sensitive paint images of rotating surfaces. *AIAA Journal*, 52(9):2045–2061, 2014.

P.C. Hansen, J.G. Nagy, and D.P. O Leary. *Deblurring Images: Matrices, Spectra, and Filtering*. Society for Industrial and Applied Mathematics, 2006.

N.E. Holgate, P.T. Ireland, and E. Romero. An experimental-numerical method for transient infrared measurement of film cooling effectiveness and heat transfer coefficient in a single test. *The Aeronautical Journal*, Royal Aeronautical Society:1–17, 2019.

B. Kirollos and T. Povey. Aerothermal optimisation of novel cooling schemes for high pressure components using combined theoretical, numerical and experimental techniques. *PhD Thesis, University of Oxford*, 2015.

B. Kirollos and T. Povey. High-accuracy infrared thermography method using reflective marker arrays. *Meas. Sci. Technol.*, 28:1–12, 2017.

B.F. Knisely, R.A. Berdanier, K.A Thole, C.W. Haldeman, J.R. Markham, J.E. Cosgrove, A.E. Carlson, and J.J. Scire. Acquisition and processing considerations for infrared images of rotating turbine blades. *ASME. J. Turbomach.*, 2021.

S. Lazzi-Gazzini, R. Schader, A.L. Kalfas, and R.S. Abhari. Infrared thermography with non-uniform heat flux boundary conditions on the rotor endwall of an axial turbine. *Meas. Sci. Technol.*, 280: 1–16, 2017.

J. Manara, M. Zips, T. Stark, M. Arduini, H.-P. Erbert, A. Tutschke, A. Hallam, J. Hanspal, M. Langley, D. Hodge, and J. Hartmann. Long wavelength infrared radiation thermometry for non-contact temperature measurements in gas turbines. *Infrared Phys. Technol.*, 80:120–130, 2017.

M. Martiny, R. Schiele, M. Gritsch, A. Schulz, and S. Wittig. In situ calibration for quantitative infrared thermography. *QIRT Eurotherm Series 50*, 1996.

M. Ochs, T. Horbach, A. Schulz, R. Koch, and H.J. Bauer. A novel calibration method for an infrared thermography system applied to heat transfer experiments. *Meas. Sci. Technol.*, 20, 2009.

A. Schulz. Infrared thermography as applied to film cooling of gas turbine components. *Meas. Sci. Technol.*, 11:948, 2000.

M. Schulz and L. Caldwell. Nonuniformity correction and correctability of infrared focal plane arrays. *Infrared Phys. Technol.*, 36:763–777, 1995.